IEEE Access
Multidisciplinary | Rapid Review | Open Access Journal

Received June 19, 2020, accepted August 17, 2020, date of publication August 24, 2020, date of current version September 4, 2020.

Digital Object Identifier 10.1109/ACCESS.2020.3018868

Interpretation and Analysis of Target Scattering From Fully-Polarized ISAR Images Using Pauli Decomposition Scheme for Target Recognition

SEVKET DEMIRCI, OZKAN KIRIK, AND CANER OZDEMIR, (Member, IEEE)
Department of Electrical and Electronics Engineering, Mersin University, 33343 Mersin, Turkey
Corresponding author: Sevket Demirci (sdemirci@mersin.edu.tr)

This work was supported in part by the Mersin University Scientific Research Unit under Grant 2015-TP3-1160.

ABSTRACT An assessment of polarimetric inverse synthetic aperture radar (Pol-ISAR) imaging is accomplished for realistic target models with the use of our recently developed high-frequency radar cross-section simulator tool called PREDICS. X-band, narrow-angle and full-polarimetric ISAR data for the CAD models of the well-known test object SLICY and a ground vehicle, namely a backhoe loader are analyzed to infer their structural characteristics. Experimental data obtained from a tower-turntable ISAR measurements of a T-72 tank target have also been utilized to assess the validity of the simulator. First, the intensity images in linear and circular polarization bases are directly utilized to evaluate the data quality and to characterize target features for classification. Then, the Pauli image decomposition scheme is applied to separate the basic scattering mechanisms occurring at target pixels. The identifiable canonical target forms are successfully extracted as single, double and multi-bounce scattering mechanisms that are pinpointed at their true locations. The results indicate that PREDICS is able to generate high-fidelity synthetic Pol-ISAR signatures of complex targets whereby successful interpretation of innumerous target scattering mechanisms and features can be achieved through Pauli decomposition scheme for classification purposes.

INDEX TERMS PREDICS radar cross-section (RCS) simulator, inverse synthetic aperture radar (ISAR), Pauli decomposition, polarimetric ISAR.

I. INTRODUCTION

Most synthetic aperture radar (SAR) systems are now utilizing polarimetric diversity in data collection. This is mainly because radar polarimetry provides unique information for the retrieval of targets' physical parameters such as dihedral and surface like scatterers [1], [2]. Polarimetric SAR (Pol-SAR) has already proven its effectiveness in several applications from terrain classification to image contrast enhancement [3], [4]. Inverse synthetic aperture radar (ISAR) systems; on the other hand, traditionally utilize single-polarization imagery in magnitude domain for target recognition tasks [5]–[8]. However, highly variable image signatures, caused by complex structures of typical ISAR targets, i.e., aircrafts, tanks and ships, along with wide-variability in observations, make interpretation of this conventional analysis difficult. [9].

The associate editor coordinating the review of this manuscript and approving it for publication was Davide Comite.

The sensitivity of polarimetric backscattering to target structures (orientations, shapes, sizes) make polarimetric ISAR (Pol-ISAR) a promising tool for target recognition applications [10]–[21]. This demands for a target (or polarimetric scattering) decomposition scheme. The purpose of target decomposition is to separate and classify the total scattering measured by the radar into scattering responses of simple or canonical objects for an easier physical interpretation [22]–[26]. To date, there is limited but growing interest in Pol-ISAR imaging as the demand for target classification tasks have been increasing [10]–[21]. Some experiments have been conducted to study the applicability of target decomposition schemes for high resolution Pol-ISAR or polarimetric radar cross-section (RCS) data. For example, the effectiveness of the Huynen-Euler [15], [16], the Pauli [17]–[21], the Krogager [19]–[21] and the Cameron [19]–[21] decompositions have been evaluated by exploiting many benchmark reflectors and scale models of complex vehicles such as tanks and boats [15]–[21]. The principal findings of these

studies agree with the theoretical expectations, but the work completed thus far is introductory and little laboratory work has dealt with the scattering behavior of more realistic targets.

An assessment of the utility of Pol-ISAR in improving recognition of complex targets, can also be made by means of simulation studies [27]–[30]. This could serve as a ground-truth validation of the relevant techniques, mainly the ones related to target decompositions. Among the few published examples, polarization properties of an unmanned aerial vehicle model have been investigated in [31], [32] by fusing the three decomposition methods. Toward this direction, this article makes use of the simulated Pol-ISAR imagery to characterize the backscattering signatures of a SLICY (Sandia Laboratory Implementation of Cylinders) object and a stationary ground vehicle, i.e., a backhoe loader. Simulation studies have been carried out with our recently developed high-frequency RCS simulator tool, called PREDICS [27]–[29] that is based on shooting and bouncing ray (SBR) technique [33], [34] and capable of gathering full linear polarization (LP) data. An analysis of the real experimental data of a T-72 tank resulted from turntable-based ISAR measurements has also been made to evaluate the validity of the electromagnetic code. The intensity images in LP basis, synthetically generated circular polarization (CP) basis and the Pauli decomposition images are analyzed to recognize the targets' identifiable features from the constructed Pol-ISAR images and from Pauli images. The findings of these analyses and detailed discussions are presented.

II. THEORY

A. SCATTERING MATRIX

Most polarimetric radars operate in linear horizontal (H) and/or vertical (V) basis, measuring up to four channels, i.e., HH, HV, VH and VV, with the first and second letters represent transmit and receive polarizations, respectively. The monostatic backscattering electric field from a target measured at far-field is completely described by the 2×2 polarization scattering matrix $[S]$ via

$$\vec{E}^r = \frac{e^{-j2kr}}{r}[S]\vec{E}^t$$
$$\begin{bmatrix} E_H^r \\ E_V^r \end{bmatrix} = \frac{e^{-j2kr}}{r}\begin{bmatrix} S_{HH} & S_{HV} \\ S_{VH} & S_{VV} \end{bmatrix}\begin{bmatrix} E_H^t \\ E_V^t \end{bmatrix} \quad (1)$$

which links the transmitted (incident) electric field vector $\vec{E}^t$ to the received (scattered) electric field vector $\vec{E}^r$. The propagation term e^{-jkr}/r, in which k being the wavenumber and r being the distance between target and antenna, is not a target related parameter and thus often normalized out. The elements of $[S]$ are the complex scattering amplitudes $S_{ij} = |S_{ij}|\, e^{(j\varphi_{ij})}$ which are dependent only on the target characteristics, for a fixed viewing geometry (azimuth angle ϕ, elevation angle θ) and frequency. The diagonal and off-diagonal elements are called as co-polarized (co-pol) and cross-polarized (cross-pol) terms, respectively.

TABLE 1. Monostatic polarization scattering matrices of elementary scatterers.

Target	Linear-H/V Basis $[S^{LP}] = \begin{bmatrix} S_{HH} & S_{HV} \\ S_{VH} & S_{VV} \end{bmatrix}$	Circular- L/R Basis $[S^{CP}] = \begin{bmatrix} S_{LL} & S_{LR} \\ S_{RL} & S_{RR} \end{bmatrix}$
Odd-bounce targets (flat plates, trihedrals and curved surfaces)	$\begin{bmatrix} 1 & 0 \\ 0 & 1 \end{bmatrix}$	$\begin{bmatrix} 0 & 1 \\ 1 & 0 \end{bmatrix}$
Vertical dihedral	$\begin{bmatrix} -1 & 0 \\ 0 & 1 \end{bmatrix}$	$\begin{bmatrix} -1 & 0 \\ 0 & -1 \end{bmatrix}$
Horizontal dihedral	$\begin{bmatrix} 1 & 0 \\ 0 & -1 \end{bmatrix}$	$\begin{bmatrix} 1 & 0 \\ 0 & 1 \end{bmatrix}$
Vertical pole	$\begin{bmatrix} 0 & 0 \\ 0 & 1 \end{bmatrix}$	$\frac{1}{2}\begin{bmatrix} -1 & 1 \\ 1 & -1 \end{bmatrix}$
Horizontal pole	$\begin{bmatrix} 1 & 0 \\ 0 & 0 \end{bmatrix}$	$\frac{1}{2}\begin{bmatrix} 1 & 1 \\ 1 & 1 \end{bmatrix}$
45° inclined pole	$\frac{1}{2}\begin{bmatrix} 1 & 1 \\ 1 & 1 \end{bmatrix}$	$\frac{1}{2}\begin{bmatrix} j & 1 \\ 1 & -j \end{bmatrix}$

For monostatic configurations, $[S]$ becomes symmetric, i.e., $S_{HV} = S_{VH}$ for all reciprocal scattering media.

The scattering matrix can also be measured in any basis of orthogonal polarizations, such as left (L)-right (R) circular basis. It is important to note that the physical scattering information inside $[S]$ remains unchanged even it is transformed to any polarization basis of LP, CP or any other type. As an example, the transformation from linear to circular basis can be readily obtained as

$$\left[S^{CP}\right] = [U]\left[S^{LP}\right][U]^T \quad (2)$$

where

$$[U] = \frac{1}{\sqrt{2}}\begin{bmatrix} 1 & j \\ 1 & -j \end{bmatrix} \quad (3)$$

and $[U]^T$ is the transpose of $[U]$.

Table 1 shows the polarization scattering matrices of some canonical targets for both LP and CP bases [1].

B. BACKSCATTERING FROM A COMPLEX TARGET

Each pixel in a focused Pol-ISAR imagery retains the four complex elements of $[S]$ measured for different polarizations. It is well-known that man-made objects give rise to completely polarized scattered waves, and hence named as deterministic or coherent targets. In high frequency approximation, the backscattered signal from a coherent target is dominated by local scattering centers [5]. Also, the scattering mechanisms occurring around these target regions tend to be highly complex due to the complicated target structures. This arises from the coherent addition of contributions from single, double, triple and higher-order bounce scattering mechanisms. In such cases, target decomposition approaches can be utilized to decouple this superposition of scattering mechanisms. In particular, coherent decompositions utilize directly the polarization scattering matrix of $[S]$ and express it with a combination of simpler (such as canonical) responses for an easier interpretation. Among these decomposition techniques, the most basic and the efficient one is the so-called the

Pauli decomposition scheme that is successfully employed in imaging applications such as SAR urban monitoring.

C. THE PAULI DECOMPOSITION

In radar polarimetry, two basis matrix sets are commonly used: The Pauli basis matrices Ψ_P and the lexicographic basis matrices Ψ_L [1]. The explicit expression of Ψ_P for the monostatic case (i.e., $S_{HV} = S_{VH}$) is given by the following three 2×2 matrices

$$\Psi_{P3} = \{[S]_a, [S]_b, [S]_c\} = \left\{\sqrt{2}\begin{bmatrix}1 & 0\\ 0 & 1\end{bmatrix}, \sqrt{2}\begin{bmatrix}1 & 0\\ 0 & -1\end{bmatrix}, \sqrt{2}\begin{bmatrix}0 & 1\\ 1 & 0\end{bmatrix}\right\} \quad (4)$$

The Pauli decomposition expresses the measured $[S]$ in this basis as

$$[S] = \begin{bmatrix}S_{HH} & S_{HV}\\ S_{HV} & S_{VV}\end{bmatrix} = k_1 [S]_a + k_2 [S]_b + k_3 [S]_c \quad (5)$$

where

$$k_1 = \frac{S_{HH} + S_{VV}}{\sqrt{2}}, \quad k_2 = \frac{S_{HH} - S_{VV}}{\sqrt{2}}, \; k_3 = \sqrt{2} S_{HV} \quad (6)$$

are the complex coefficients that correspond to the weights of the associated basis matrix. From Eq. (6), the span (i.e., total power) of $[S]$ can also be described in terms of these coefficients as

$$\begin{aligned}\text{span}([S]) &= |S_{HH}|^2 + |S_{VV}|^2 + 2|S_{HV}|^2\\ &= |k_1|^2 + |k_2|^2 + |k_3|^2 . \end{aligned} \quad (7)$$

The interpretation of the Pauli decomposition can be made by considering the basis matrices. Note that each matrix represents isotropic scattering mechanisms, that is $|S_{HH}| = |S_{VV}|$. The first matrix $[S]_a$ with $S_{HH} = S_{VV}$ and $S_{HV} = S_{VH} = 0$ can be interpreted as the scattering matrix of an ''odd-bounce'' scatterer such as caused by spheres, flat surfaces and trihedral corner reflectors (TCRs). Therefore, as an example, k_1 and $|k_1|^2$ represents the proportion of the contributions of such scatterers in the measured data, in voltage and power terms, respectively. The second matrix $[S]_b$ involves 180° phase difference between the co-pol terms and corresponds to the scattering matrix of a dihedral rotated at 0° about the line-of-sight (LOS). It indicates ''double-bounce'' or ''even-bounce'' scattering such as observed from dihedral corner structures. The last matrix $[S]_c$ corresponds to the scattering matrix of a dihedral rotated 45° about the LOS. Noting that this matrix is defined with respect to LP basis, it represents a scatterer that transforms the incident polarization into its orthogonal state. This term is sometimes associated with ''volume scattering'' such as from trees or even-bounce scattering from 45° oriented targets. However, this may not always fully account the real phenomena. It is actually a representative of the loss of symmetry of $[S]$ and thus disappears for reciprocal backscattering cases.

Finally, the information in $[S]$ is usually displayed and interpreted in a single red-green-blue (RGB) image, by assigning blue, red and green colors to the amplitudes of the first, second and third components, respectively.

III. NUMERICAL EXPERIMENTS

All the electromagnetic scattering simulation experiments have been carried out by our recently developed high-frequency physical electromagnetic simulator tool called PREDICS [27]–[29]. PREDICS is based on SBR technique [33], [34] that utilized ray launching with geometric optics (GO) theory and the application of the physical optics (PO) theory together with the physical theory of diffraction (PTD). The detailed theoretical derivation behind PREDICS and its accuracy validation studies in predicting the electromagnetic scattering and/or radar RCS from benchmark targets can be reached from [27], [28] and [29] and will not be repeated here. PREDICS can compute fully-polarimetric electromagnetic backscattering from electrically large and complex objects with high accuracy which is followed with generation of RCS and ISAR imagery.

The RCS simulations of test object and the targets have been carried out using the using PO (physical optics) + SBR (shooting and bouncing ray) + PTD (Physical Theory of Diffraction) solver of PREDICS for all the polarimetric signatures; i.e., S_{HH}, S_{HV}, S_{VH} and S_{VV}.

A. TEST OBJECT: SLICY

To examine the performance of the simulator and validate the polarization scattering matrices of a number of canonical targets, the well-known SLICY object that contains several radar reflector shapes such as; a short open cylinder (A; top-hat), a tall closed cylinder (B; top-hat), a TCR (C), two step-like dihedrals (D and E), a quarter cylinder (F) and a flat plate (G) has been chosen as the test object as its CAD model can be seen in Fig. 1(a). SLICY has extensions of 7.56 m, 8.50 m and 5.24 m in x, y and z directions, respectively. The reason for selecting SLICY as a test object is that its certain primitive structures can support unique electromagnetic scattering features including single, double, triple and multiple bounces as labelled in Fig.1(a) from A to G. The simulations were carried out at the center frequency of 12 GHz and for the two different look angles of $(\theta^i = 90°, \phi^i = 0°)$ and $(\theta^i = 75°, \phi^i = 0°)$. To achieve ISAR image resolutions of approximately 15 cm in both range and cross-range dimensions, the frequency bandwidth of 1 GHz and angular look-extend of 4.5° were used for a total of distinct 100 frequencies and 100 look angles.

1) EXPERIMENT #1

In the first experiment, the target was illuminated around the look angle of $(\theta^i, \phi^i) = (90°, 0°)$ as depicted in Fig. 1(a). For this look-angle, some dominant backscattering mechanisms are illustrated in Fig. 1(b). While odd-bounce mechanisms such as single and triple ones are depicted in blue color, the double-bounce mechanisms are shown in red color.

After applying the small-bandwidth, small-angle ISAR image construction routine [5] which is based on simply taking the two-dimensional (2D) inverse Fourier transform of the data, the resultant benchmark ISAR (or RCS) images

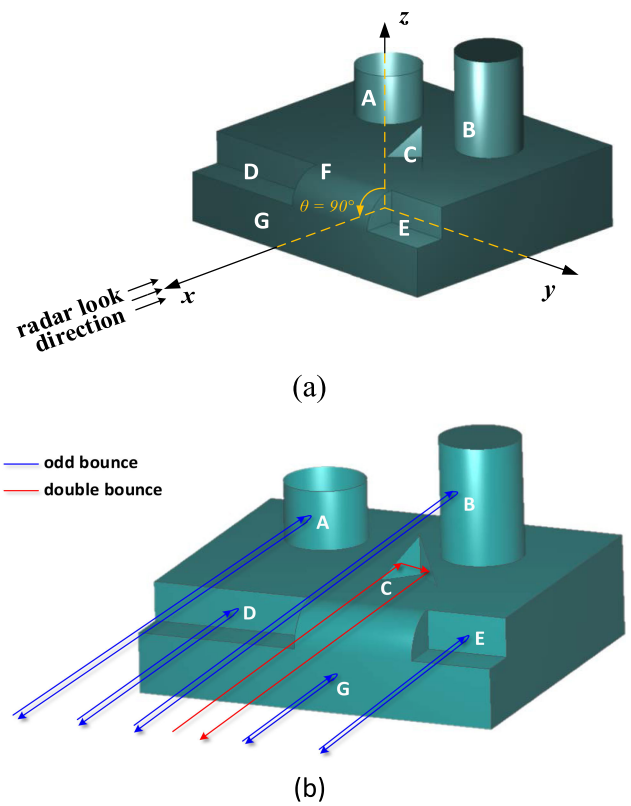

FIGURE 1. (a) Geometry for the full-polarimetric RCS/ISAR simulation of the SLICY object for the aspect angle $\left(\theta^i = 90°, \phi^i = 0°\right)$, (b) Some dominant backscattering mechanisms from the SLICY object for the illustrated aspect angle.

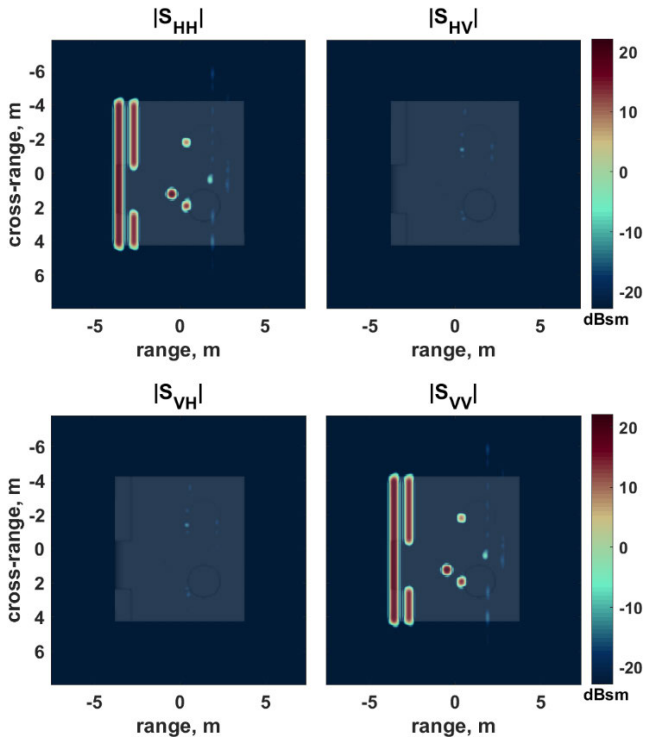

FIGURE 2. LP ISAR images of the SLICY object for the aspect angle $\left(\theta^i = 90°, \phi^i = 0°\right)$.

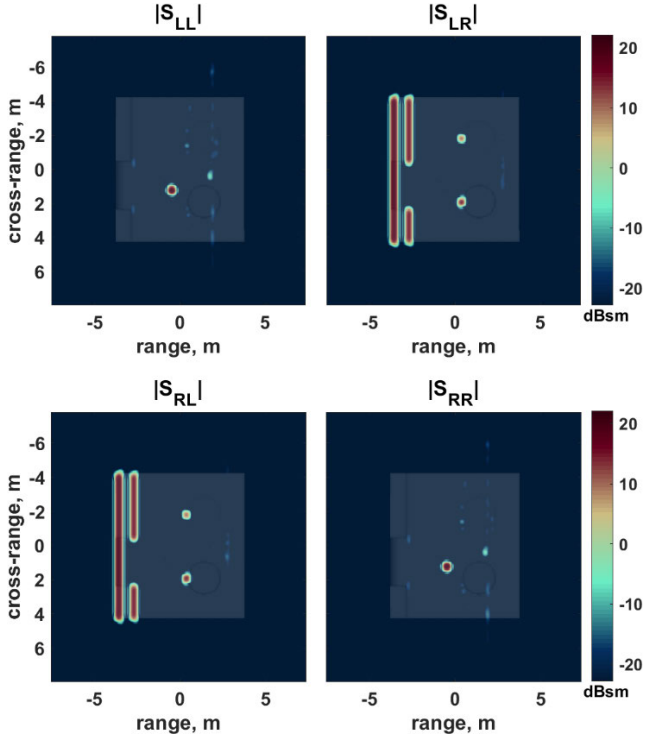

FIGURE 3. CP ISAR images of the SLICY object for the aspect angle $\left(\theta^i = 90°, \phi^i = 0°\right)$.

for the LP and CP bases are acquired as shown in Fig. 2 and Fig. 3, respectively. LP images in Fig. 2 demonstrate that all the notable backscattered powers are shown up only in co-pol ($|S_{HH}|$ and $|S_{VV}|$) images, whereas the cross-pol ($|S_{HV}|$ and $|S_{VH}|$) images have provided very low power levels. This is expected since most of the canonical objects on SLICY supports co-pol mechanisms and the only structures that can produce some cross-pol mechanisms are the cylinders (A and B) owing to edge diffractions. The highest reflection was observed from the TCR (C) with a peak RCS value of 22 dBsm. Furthermore, specular backscattering mechanisms from the flat surfaces (D, E and G) are seen in the form of straight-line radar signatures, while the illuminated surfaces of the two cylinders (A and B) and TCR (C) are shown up as point-like signatures. The curved surface of the quarter cylinder (F) around the step region do not offer sufficient scattering power to appear within the dynamic range of the display for this particular look-angle.

These RCS images; however, do not discriminate between odd-bounce and double-bounce scattering. On the other hand, CP images that are presented in Fig. 3 clearly separate the reflectors that have odd-bounce and double-bounce characteristics. To clarify this, first note that cross-pol (either $|S_{LR}|$ or $|S_{RL}|$) represents odd-bounce scattering whereas co-pol ($|S_{LL}|$ and $|S_{RR}|$) represents double or even-number of bounces scattering for a circularly polarized wave. Next, also note that at this frontal view of SLICY, all the reflectors except the TCR, are expected to give rise to odd-bounce scattering. The TCR; on the other hand, behaves like a horizontal

TABLE 2. Attributes of slicy reflectors for the Experiment #1: description, structure/scattering mechanism in accordance with the aspect angle and the computed average rcs and scattering matrices for linear and circular bases.

Description (Label)	Structure (Scattering Mechanism)	Linear-H/V Basis		Circular- L/R Basis	
		Scattering Matrix $\begin{bmatrix} S_{HH} & S_{HV} \\ S_{VH} & S_{VV} \end{bmatrix}$	RCS (dBsm) $\begin{bmatrix} \sigma_{HH} & \sigma_{HV} \\ \sigma_{VH} & \sigma_{VV} \end{bmatrix}$	Scattering Matrix $\begin{bmatrix} S_{LL} & S_{LR} \\ S_{RL} & S_{RR} \end{bmatrix}$	RCS (dBsm) $\begin{bmatrix} \sigma_{LL} & \sigma_{LR} \\ \sigma_{RL} & \sigma_{RR} \end{bmatrix}$
Short cylinder (A)	Cylinder surface (single-bounce)	$\begin{bmatrix} 2.9e^{j73^\circ} & 0.05e^{j173^\circ} \\ 0.05e^{j173^\circ} & 2.9e^{j73^\circ} \end{bmatrix}$	$\begin{bmatrix} 9.2 & -26 \\ -26 & 9.2 \end{bmatrix}$	$\begin{bmatrix} 0.05e^{j76^\circ} & 3.05e^{j73^\circ} \\ 3.05e^{j73^\circ} & 0.05e^{-j90^\circ} \end{bmatrix}$	$\begin{bmatrix} -26 & 9.7 \\ 9.7 & -26 \end{bmatrix}$
Tall cylinder (B)	Cylinder surface (single-bounce)	$\begin{bmatrix} 5.6e^{j120^\circ} & 0.02e^{-j52^\circ} \\ 0.02e^{-j70^\circ} & 5.6e^{j120^\circ} \end{bmatrix}$	$\begin{bmatrix} 15 & -34 \\ -34 & 15 \end{bmatrix}$	$\begin{bmatrix} 0.02e^{-j135^\circ} & 5.7e^{j165^\circ} \\ 5.7e^{j165^\circ} & 0.02e^{j99^\circ} \end{bmatrix}$	$\begin{bmatrix} -34 & 15.1 \\ 15.1 & -34 \end{bmatrix}$
TCR (C)	Dihedral (double-bounce)	$\begin{bmatrix} 12.3e^{j54^\circ} & 7.9\times10^{-6}e^{-j147^\circ} \\ 2.4\times10^{-5}e^{-j39^\circ} & 12.3e^{-j125^\circ} \end{bmatrix}$	$\begin{bmatrix} 21.8 & -102 \\ -92 & 21.8 \end{bmatrix}$	$\begin{bmatrix} 12.2e^{j98^\circ} & 0.05e^{-j37^\circ} \\ 0.05e^{-j37^\circ} & 12.2e^{j98^\circ} \end{bmatrix}$	$\begin{bmatrix} 21.7 & -26 \\ -26 & 21.7 \end{bmatrix}$
Step-like dihedral (D-E)	Flat surface (single-bounce)	$\begin{bmatrix} 6.1e^{-j127^\circ} & 9.6\times10^{-7}e^{-j14^\circ} \\ 9.1\times10^{-7}e^{-j14^\circ} & 6.1e^{-j127^\circ} \end{bmatrix}$	$\begin{bmatrix} 15.7 & -120 \\ -121 & 15.7 \end{bmatrix}$	$\begin{bmatrix} 0.01e^{j82^\circ} & 6.1e^{j142^\circ} \\ 6.1e^{j142^\circ} & 0.01e^{j82^\circ} \end{bmatrix}$	$\begin{bmatrix} -40 & 15.7 \\ 15.7 & -40 \end{bmatrix}$
Flat plate (G)	Flat surface (single-bounce)	$\begin{bmatrix} 9.6e^{j128^\circ} & 5\times10^{-7}e^{j179^\circ} \\ 2.1\times10^{-7}e^{j147^\circ} & 9.6e^{j128^\circ} \end{bmatrix}$	$\begin{bmatrix} 19.6 & -126 \\ -133 & 19.6 \end{bmatrix}$	$\begin{bmatrix} 0.03e^{j119^\circ} & 9.6e^{-j141^\circ} \\ 9.6e^{-j141^\circ} & 0.03e^{j119^\circ} \end{bmatrix}$	$\begin{bmatrix} -30.4 & 19.6 \\ 19.6 & -30.4 \end{bmatrix}$

dihedral for the look-aspect of $(\theta^i, \phi^i) = (90^\circ, 0^\circ)$ and thus turns to a double-bounce scatterer with co-pol signatures.

For a quantitative inspection of the signatures of SLICY's sub-structures, the scattering matrix and RCS values were extracted from the simulated images by using a rectangular window centered at the target's peak response. Table 2 lists the averages of these values for LP and CP bases. To aid interpretation, the structure and the expected scattering mechanisms for each reflector which are indicated on the CAD model given in Fig. 1(b) are also included in the table. The computed complex scattering amplitudes and thus RCS values are found to be consistent with the theoretical ones given in Table 1. As an example, the scattering matrix of TCR for LP basis contains nearly 180° phase difference between S_{HH} and S_{VV} channels, thereby indicating a double-bounce scattering which is expected for the current view angle. All the other primitive shapes show odd-bounce scattering, which generates strong reflections in co-pol channels of LP and cross-pol channels of CP.

Afterwards, the Pauli decomposition given in Eq. (5) and (6) was applied to the scattering matrices of the image pixels. The obtained Pauli image with RGB color coding is shown in Fig. 4(a). The TCR produces a red color, again indicating a double-bounce mechanism. The flat surface (G) and the two step-like dihedrals (D and E) only produce specular reflections and therefore, they showed out in blue color as expected. In a similar manner, cylinders' side surfaces also support only the singular reflection for this particular look-angle. Hence, their Pauli responses produce blue-color as depicted in Fig. 4(a). These observations show good agreement with the expected polarimetric scattering responses of elementary targets on SLICY. The total power (span) values were also calculated from the Pauli decomposition via Eq. 7. The backscattering coefficients are normalized to the maximum value of the four polarization images and displayed within a 50 dB dynamic range, as shown in Fig. 4(b).

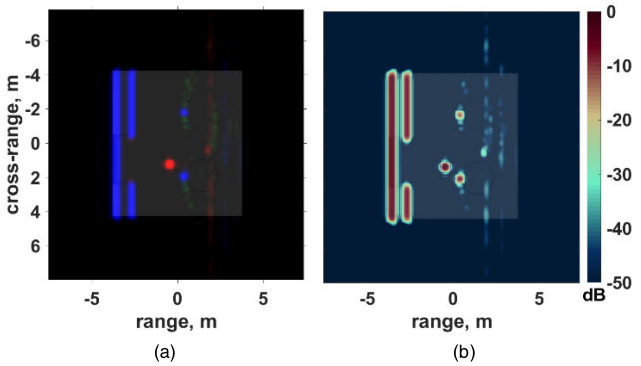

FIGURE 4. (a) Pauli RGB image with $R = |S_{HH} - S_{VV}|$, $G = |S_{HV} + S_{VH}|$, $B = |S_{HH} + S_{VV}|$, (b) total power image of the SLICY object for the aspect angle $(\theta^i = 90^\circ, \phi^i = 0^\circ)$.

The highest power values for the TCR (C), large cylinder (B) and small cylinder (A) are identified as; 0, −12.6 and −6.9 dBsm, respectively. The flat surfaces with labels (D-E) and (G) are also recognized to have around −6.3 and −2.5 dBsm levels, respectively. Also, there exist some numerical noise of about −30dB that can be seen around 2m range location in these images due to PREDICS's numerical simulation and small-bandwidth small angle ISAR reconstruction algorithm approximations.

2) EXPERIMENT #2

In this experiment, the aspect angle was chosen as $(\theta^i = 75^\circ, \phi^i = 0^\circ)$ in order to evaluate the angle-dependent effects on scattering characteristics. SLICY's view for this look angle is pictured in Fig. 5(a) while some dominant backscattering mechanisms are depicted in Fig. 5(b) by representing again, odd-bounce and double-bounce mechanisms with blue and red colors, respectively.

The reconstructed ISAR images in LP basis are shown in Fig. 6. As expected, co-pol ($|S_{HH}|$ and $|S_{VV}|$) ISAR images

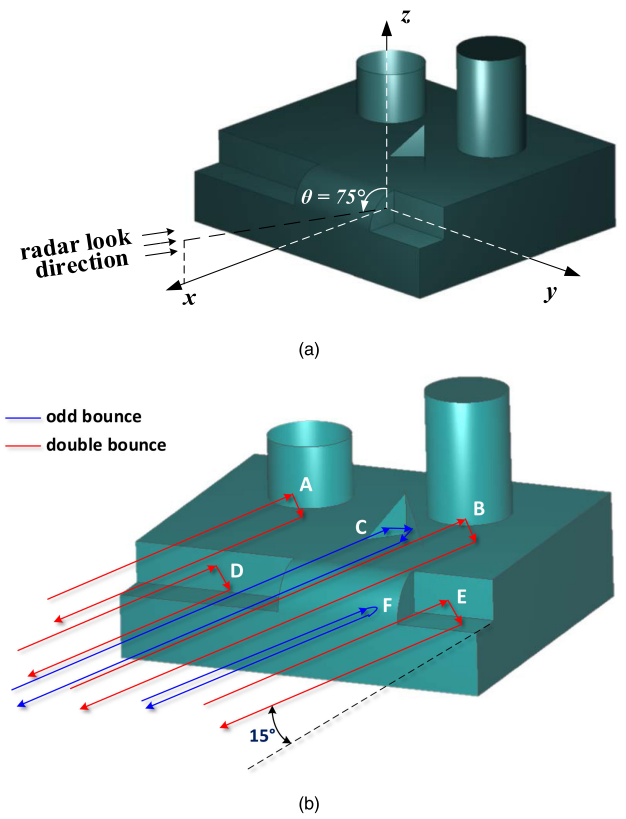

FIGURE 5. (a) Geometry for full-polarimetric RCS/ISAR simulation of the SLICY object for the aspect angle $\left(\theta^i = 75°, \phi^i = 0°\right)$, (b) Some dominant backscattering mechanisms from the SLICY object for the illustrated aspect angle.

present high RCS values whereas the cross-pol ($|S_{HV}|$ and $|S_{VH}|$) ISAR images provide much weaker powers that cannot be observed at -20 dBsm RCS level. Since the electromagnetic illumination is from an oblique incidence to the SLICY object, the scattering types are quite different from Experiment #1. The strongest return is from the trihedral such that the RCS value is about 25 dBsm as it can be read from the co-pol images in Fig. 6. Since the step regions (D & E) behave like dihedral corner reflectors, they also provide significant backscattered power so that the backscattered RCS values at the levels around 10 dBsm in both co-polar images. There exist double-scattering mechanisms between the cylinders (region A & B) and the top-surface of SLICY. These mechanisms show up in the co-pol ($|S_{HH}|$ and $|S_{VV}|$) ISAR images as their RCS values are around 8.8 dBsm. Another important scattering mechanism is from the circular curved surface (F) that is clearly pointed out in the co-pol ISAR images with the RCS level of around -3.5 dBsm. It is also obvious that specular (single-bounce) reflections from the steps regions in Experiment #1 are not available for this study due to oblique incidence wave illumination; therefore, they do not show up in the constructed ISAR images.

For the experiment #2, the CP images in Fig. 7 present completely different characteristics than that of experiment #1 (see Fig. 3 for comparison). These circular images have

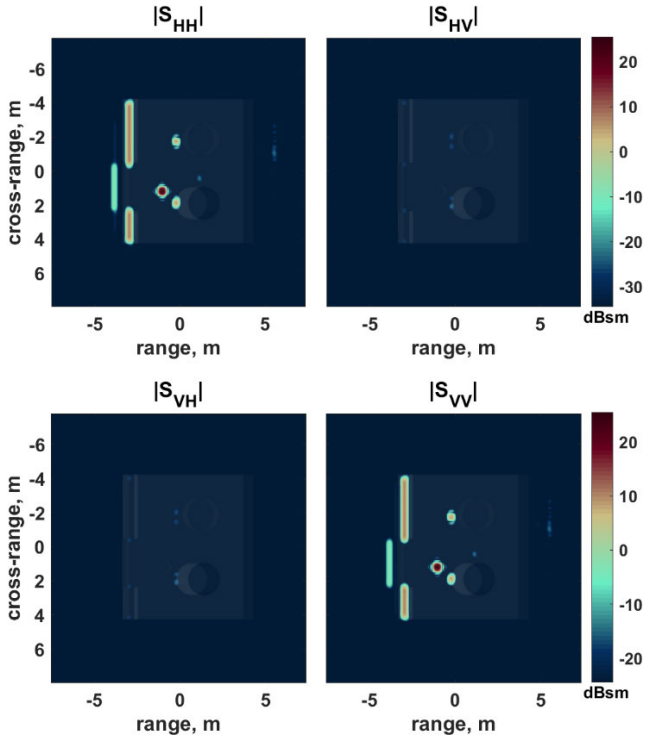

FIGURE 6. LP ISAR images of the SLICY object for the aspect angle $\left(\theta^i = 75°, \phi^i = 0°\right)$.

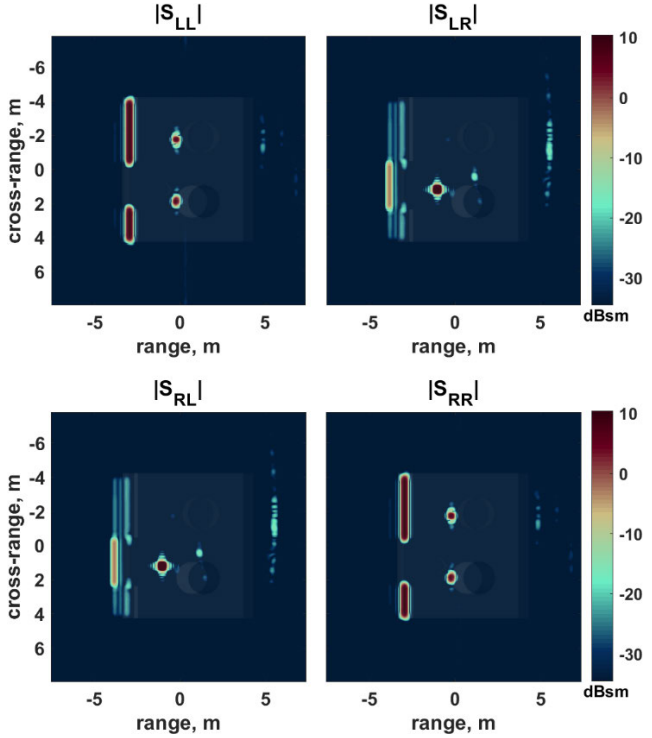

FIGURE 7. CP ISAR images of the SLICY object for the aspect angle $\left(\theta^i = 75°, \phi^i = 0°\right)$.

the useful property of providing characterization of electromagnetic reflectivity, so discriminating the single, double and multi-bounce scattering mechanisms. The double-bounce mechanisms from the step regions and from the cylinder-body

TABLE 3. Attributes of slicy reflectors for the experiment #2: description, structure/scattering mechanism in accordance with the aspect angle and the computed average rcs and scattering matrices for linear and circular bases.

Description (Label)	Structure (Scattering Mechanism)	Linear-H/V Basis		Circular- L/R Basis	
		Scattering Matrix $\begin{bmatrix} S_{HH} & S_{HV} \\ S_{VH} & S_{VV} \end{bmatrix}$	RCS (dBsm) $\begin{bmatrix} \sigma_{HH} & \sigma_{HV} \\ \sigma_{VH} & \sigma_{VV} \end{bmatrix}$	Scattering Matrix $\begin{bmatrix} S_{LL} & S_{LR} \\ S_{RL} & S_{RR} \end{bmatrix}$	RCS (dBsm) $\begin{bmatrix} \sigma_{LL} & \sigma_{LR} \\ \sigma_{RL} & \sigma_{RR} \end{bmatrix}$
Short cylinder (A)	Dihedral (top-hat) (double-bounce)	$\begin{bmatrix} 2.7e^{-j133^\circ} & 0.005e^{-j15^\circ} \\ 0.005e^{-j15^\circ} & 2.7e^{j46^\circ} \end{bmatrix}$	$\begin{bmatrix} 8.8 & -46 \\ -46 & 8.8 \end{bmatrix}$	$\begin{bmatrix} 2.7e^{-j89^\circ} & 0.01e^{-j6.9^\circ} \\ 0.01e^{-j6.5^\circ} & 2.7e^{-j89^\circ} \end{bmatrix}$	$\begin{bmatrix} 8.6 & -40 \\ -40 & 8.6 \end{bmatrix}$
Tall cylinder (B)	Dihedral (top-hat) (double-bounce)	$\begin{bmatrix} 2.7e^{j136^\circ} & 0.03e^{j2^\circ} \\ 0.03e^{j4^\circ} & 2.7e^{-j43^\circ} \end{bmatrix}$	$\begin{bmatrix} 8.8 & -30 \\ -30 & 8.8 \end{bmatrix}$	$\begin{bmatrix} 2.7e^{j91^\circ} & 0.004e^{j60^\circ} \\ 0.004e^{j66^\circ} & 2.7e^{j91^\circ} \end{bmatrix}$	$\begin{bmatrix} 8.6 & -48 \\ -48 & 8.6 \end{bmatrix}$
TCR-(C)	Trihedral (triple-bounce)	$\begin{bmatrix} 18.1e^{-j152^\circ} & 3\times10^{-4}3e^{j6^\circ} \\ 4\times10^{-4}3e^{j4^\circ} & 18.1e^{-j152^\circ} \end{bmatrix}$	$\begin{bmatrix} 25.1 & -68 \\ -68 & 25.1 \end{bmatrix}$	$\begin{bmatrix} 0.01e^{-j134^\circ} & 18.8e^{j5.2^\circ} \\ 18.8e^{j5.2^\circ} & 0.01e^{-j138^\circ} \end{bmatrix}$	$\begin{bmatrix} -40 & 25.4 \\ 25.4 & -40 \end{bmatrix}$
Step-like dihedral (D, E)	Dihedral (step) (double-bounce)	$\begin{bmatrix} 3.1e^{j42^\circ} & 0.002e^{j4^\circ} \\ 0.002e^{j4^\circ} & 3.1e^{-j137^\circ} \end{bmatrix}$	$\begin{bmatrix} 9.8 & -54 \\ -54 & 9.8 \end{bmatrix}$	$\begin{bmatrix} 3.2e^{-j137^\circ} & 0.03e^{-j146^\circ} \\ 0.03e^{-j146^\circ} & 3.2e^{-j137^\circ} \end{bmatrix}$	$\begin{bmatrix} 10 & -30.4 \\ -30.4 & 10 \end{bmatrix}$
Quarter cylinder (F)	Cylinder surface (single-bounce)	$\begin{bmatrix} 0.67e^{-j155^\circ} & 4.7\times10^{-6}e^{-j6} \\ 4.7\times10^{-6}e^{-j7^\circ} & 0.67e^{-j157^\circ} \end{bmatrix}$	$\begin{bmatrix} -3.4 & -106 \\ -106 & -3.4 \end{bmatrix}$	$\begin{bmatrix} 0.01e^{-j175^\circ} & 0.64e^{j70^\circ} \\ 0.64e^{j70^\circ} & 0.01e^{-j175^\circ} \end{bmatrix}$	$\begin{bmatrix} -40 & -3.87 \\ -3.87 & -40 \end{bmatrix}$

region are clearly pronounced and odd-bounce mechanisms (single or triple) are filtered out in $|S_{LL}|$ and $|S_{RR}|$ ISAR images. On the other hand, the situation is reversed for the cross-pol (either $|S_{RL}|$ or $|S_{LR}|$) ISAR images. In this case, the single-bounce scattering from the curved step region (F) and the triple-bounce mechanisms from the trihedral in region (C) are amplified whereas double-bounce mechanisms are filtered out and are not present in these images. To better comprehend the scattering mechanism type discrimination between the linear H/V basis models and the circular R/L basis models for the sub-structures of SLICY are examined in detail with corresponding RCS values and scattering matrices as listed in Table 3. We can observe interesting analyses both from LP basis and from the CP basis models. The TCR sub-structure, for instance, has high RCS values for the co-pol entries for the LP basis model. However, it provides very large RCS values for the cross-pol entries for the CP basis model. This agrees with the theoretical expectation for the TCR target. In general, the simulation RCS and scattering matrix values given in Table 3 show good agreement with theory.

As the last study, the Pauli ISAR image for this experiment is formed in RGB color coding as plotted in Fig. 8(a) based on the decomposition formulas in Eq. (5) and (6). Also, the total power ISAR image is formed in Fig. 8(b). When compared to previous Pauli and total power ISAR images in the first experiment, several interesting observations are as follows:

i The TCR, step regions and cylinders provide strong RCS values in both total power images since they support all or some of single, double and multi-bounce mechanisms for both look-angle directions,

ii The single specular reflections are supported for the $\theta^i = 90^\circ$ case; but not for the $\theta^i = 75^\circ$ case; therefore, they only showed up in the first experiment's total power and Pauli ISAR images,

iii The Pauli ISAR images of first and second experiment produces totally different color value outcomes as in very good agreement with the theoretical expectations. For experiment #2, step regions (D & E) and base-cylinder regions (A & B) induce double reflections; therefore, all electromagnetic signatures from these regions showed up in red color. The TCR (C) induces triple bounces while circular curved surface (F) induces single reflection. Thus, the signatures from these parts of SLICY are represented as blue color tones in accordance with their backscattering amplitudes. The color values were completely the reverse for the first experiment since the look angle direction was $\theta^i = 90^\circ$. The TCR C) only provide double-bounces for this look-angle illumination; therefore, it produced the red color in the Pauli ISAR image that is given in Fig. 4(a). The step regions (D & E) and the cylinders (A & B) can only support single scattering mechanisms; so, corresponding ISAR image signatures are in blue in the same image.

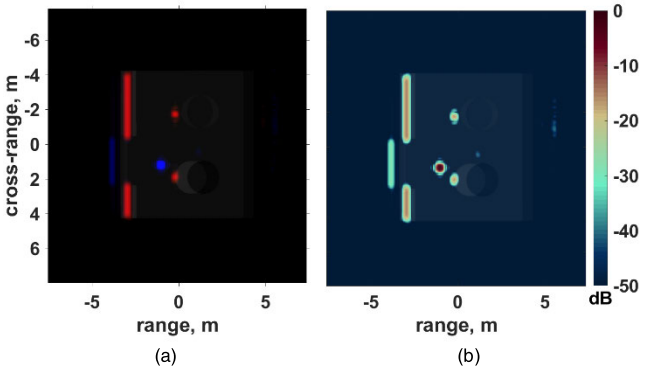

FIGURE 8. (a) Pauli RGB image with $R = |S_{HH} - S_{VV}|$, $G = |S_{HV} + S_{VH}|$, $B = |S_{HH} + S_{VV}|$, (b) normalized total power image of the SLICY object for the aspect angle $(\theta^i = 75^\circ, \phi^i = 0^\circ)$.

B. "BACKHOE LOADER OBJECT"

To examine a more complex structure, the "backhoe loader" object whose CAD file can be seen in Fig. 9 was chosen. This target has many detailed structures such that a total of 9283

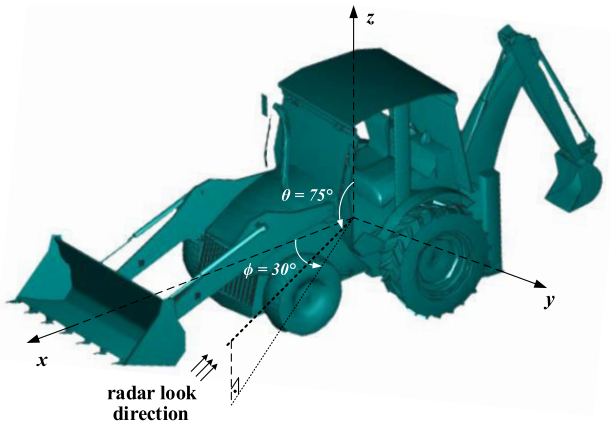

FIGURE 9. Geometry for full-polarimetric RCS/ISAR simulation of the 'Backhoe loader' object for the aspect angle $\left(\theta^i = 75°, \phi^i = 30°\right)$.

facets has been used to form cab, loader bucket, back-hoe bucket, dipper arm, tires and other many sub-structures of the object. The size of the backhoe loader is 6.33 m in length, 1.99 m in width and 2.33 m in height. Therefore, the electric size of the object becomes $189\lambda \times 60\lambda \times 70\lambda$ (at 9 GHz) which is clearly an electrically large object.

The electric field and ISAR simulations of the back-hoe loader have been performed in full-polarization using PREDICS [27]–[29] at the center frequency of $9GHz$ with 100 steps and with a total bandwidth of $1.24GHz$. The aspect angle was set to $\left(\theta^i, \phi^i\right) = (75°, 30°)$ as illustrated in Fig. 9. During the ISAR simulation, the horizontal angles were varied for equally spaced 100 steps providing a span of 7.88° horizontal angles. After the PREDICS simulation; therefore, a 2D 100 × 100 frequency-aspect raw data were collected. After applying the small-bandwidth narrow-angle ISAR imaging routine [5], ISAR images for four different polarizations were formed. LP ISAR images of the target are as depicted in Fig. 10. While the co-pol ($|S_{HH}|$ and $|S_{VV}|$) ISAR images present RCS values up to −10 dBsm, the cross-pol ($|S_{HV}|$ and $|S_{VH}|$) ISAR images provide much weaker power levels around −20dBsm at maximum. As expected, the front loader bucket has the strongest returns for both co-pol and cross-pol images since it has the characteristics of a big cavity. The front loader bucket also supports both odd and double scattering mechanisms as the incident electromagnetic wave hits inside it with inclined angles of 15° in elevation and 30° in azimuth. Furthermore, a lot of single-bounce scattering mechanisms exists at the cutting edge of the front loader bucket as their ISAR signatures are in the form of small dots with very low RCS values of around −45dBsm as it can be observed from the co-pol ($|S_{HH}|$ and $|S_{VV}|$) ISAR images of Fig. 10. The sides of the backhoe loader and the cockpit have innumerous significant signatures that may present a template for the classification of the object. The front panel grills are visible in all polarization images with an average RCS value of about −36 dBsm.

Based on the look angle direction of the backscattering collection, a portion of the grill is blocked by the left bucket

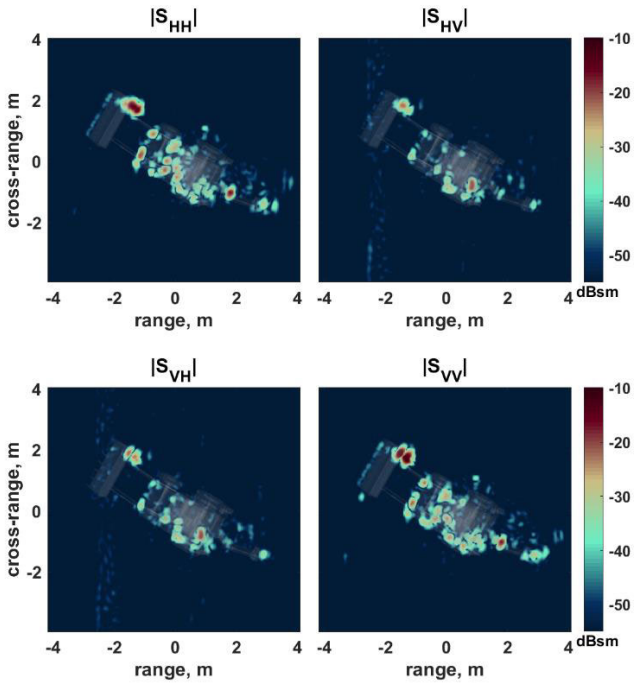

FIGURE 10. LP ISAR images of the 'Backhoe loader' object for the aspect angle $\left(\theta^i = 75°, \phi^i = 30°\right)$.

lever (see Fig. 9) and therefore; we observe a shadow region around the front panel grills. Further analysis about classification based on polarization signatures will be explained in detail while presenting circular polarization images and corresponding Pauli image.

Next, circular polarization ISAR images; i.e., *LL*, *LR*, *RL* and, *RR* that are given in Fig.11 have been constructed by utilizing full-polarization images; i.e., *HH*, *HV*, *VH* and *VV*. Although, both the co-pol (*LL* and *RR*) and cross-pol (*LR* and *RL*) images look similar, there are some discrepancies between them that can be utilized for identification purposes. It is known that co-pol circular images are more sensitive to odd-bounce mechanisms; whereas, cross-pol images tend to present double-bounce mechanisms. For instance, the cutting-edge signatures produce single-bounces; therefore, they can only be seen in the co-pol images. As another example, the back-dipper arm corner part behaves like a dihedral corner reflector according to incident wave direction. Hence, this phenomenon is noticeable in the cross-pol images of LR and RL as seen in Fig. 11.

Another analysis can be made by using the total power image that is formed in Fig. 12 based on Eq. (7): Since the total power ISAR image is formed by inclusion of each polarization contribution, the final total power ISAR has the capacity of showing all the scattering characteristics captured by any of the single polarization image. The signatures that are obtained in all polarization images are more prominent in the total power ISAR image. The front loader bucket cavity can be a good example as its signature becomes the dominant in Fig.12. The other significant backscattered signatures are from the back-dipper arm corner, front panel grills and

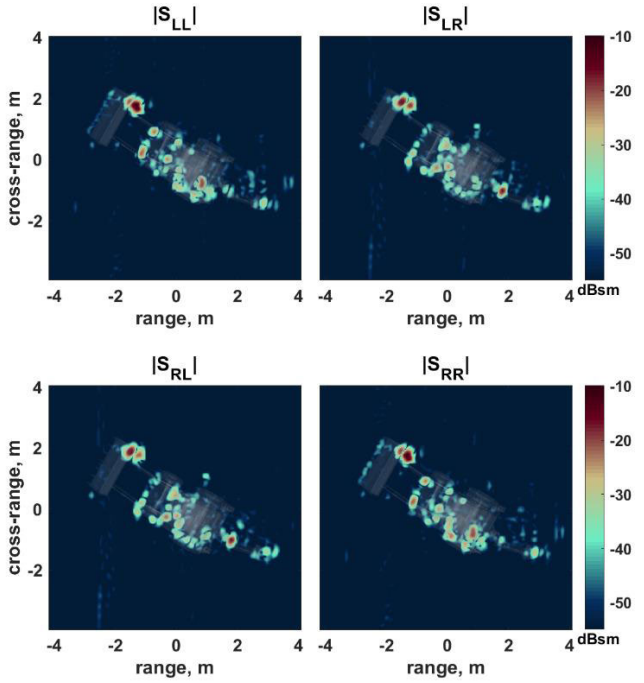

FIGURE 11. CP ISAR images of the 'Backhoe loader' object for the aspect angle $\left(\theta^i = 75°, \phi^i = 30°\right)$.

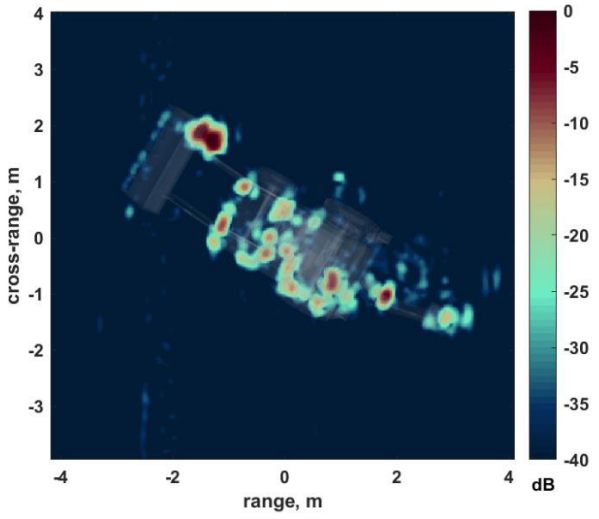

FIGURE 12. Normalized total power image of the 'Backhoe loader' object for the aspect angle $\left(\theta^i = 75°, \phi^i = 30°\right)$.

cockpit area as many scattering centers have been produced around these areas.

For the final analysis, Pauli ISAR image of backhoe loader has been constructed as plotted in Fig. 13 based on the Pauli reconstruction formulation of Eq. (5) and (6). The Pauli image has the strength of displaying all different types of scattering characteristics including odd, double and multi bounces that may correspond to the backscattering from planar surfaces, dihedral/trihedral type structures, curved surfaces etc. For the particular Pauli ISAR image in Fig. 13, innumerous different scattering features can be apparently extracted as some

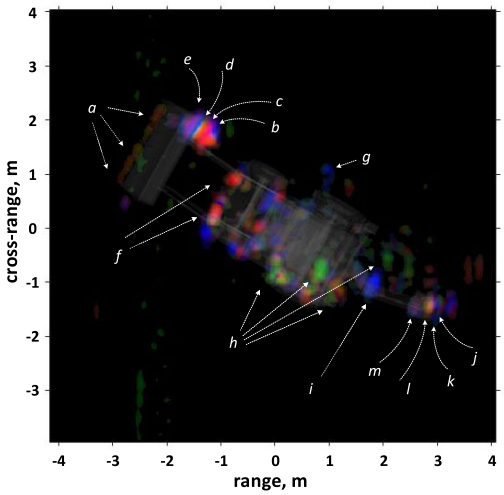

FIGURE 13. Pauli RGB image with $R = |S_{HH} - S_{VV}|$, $G = |S_{HV} + S_{VH}|$, $B = |S_{HH} + S_{VV}|$, of the 'Backhoe loader' object for the aspect angle $\left(\theta^i = 75°, \phi^i = 30°\right)$.

of them are labelled from (a) to (m) as can be seen from the image. The scatterings from the cutting edges of front loader bucket (labelled as "a'' in Fig. 13) are shown up as red color since they cause double reflection as illustrated in Fig. 14(a). The inner cavity of the front loader bucket has many interesting scattering features including single, double, triple and multiple bounce mechanisms as pictured in Fig. 14(b); therefore, the Pauli image in Fig. 13 provides blue color for odd bounce (labelled as "b''), red color for double bounce (labelled as "c$''$), violet color for combination of odd-and-double bounces (labelled as "e'') and white color for combination of odd, double and multiple bounces (labelled as "d''). The tone of each color is in fact is formed by the energy contribution of each scattering mechanism. This situation can easily be observed from the region that is labelled as "e" in the Pauli image of Fig. 13. It is fairly noticed that this region has a color spectrum that changes from light blue to violet and violet to red since this region consists of plentiful different bounce mechanisms as some of them are indicated in Fig. 14(b). The panel with metal grids in front of the motor chassis that is labelled as "f" in Fig. 13 have both red and blue color signatures in the Pauli image indicating double and odd-bounce mechanisms, respectively. The blue signature (labelled as "g'') that is a little bit away from the body of the wheeler loader corresponds to the rear mirror and its holding structure. While tracing rays towards the back-wheel region, the wheel hood and the tire create a close multi bouncing environment as labelled as "h". By this way the back-wheel region is colored with green that indicates multi-bounce mechanism. Similar argument can also be made when the rays go inside the driver cabinet and make a lot of scattered and deflected multi-bounce mechanisms. These are also showed up in green color and indicated with "h". We can also see some green colored "h" signatures that are located out of the cabinet body along the opposite direction of ISAR look-angle direction. This is another proof that these

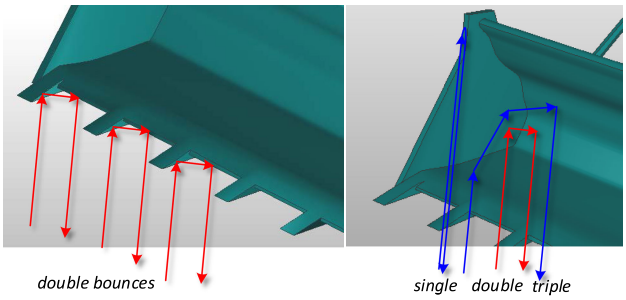

FIGURE 14. Some interesting scattering characteristics from front loader bucket (a) double reflections from the cutting edges, and (b) combination of single, double and triple reflections.

image signatures are due to numerous consecutive bounce mechanisms. Because, it is well known from ISAR theory that multiple reflections showed up in the ISAR image as late returns in the range direction [5]. Another blue color region signature (labelled as "*i*") can be noted for the dipper arm elbow as this part of the wheeler loader provides single-bounce mechanism for the look angle direction of the radar. Lastly, another interesting color signatures similar to the ones from the front loader bucket, labelled as "*j, k, l*" and *"n"*, occur from the backhoe bucket cavity. Again, it is clearly observed blue, red, violet and white colored signatures that are responsible for odd, double, combination of odd-and-double, and combination of deflected odd-and-double-and-multiple reflections, respectively.

IV. REAL EXPERIMENT

In order to check the validity of the results of PREDICS simulator and Pauli decomposition, data analysis of a real experiment has been made. For this purpose, we have exploited the Georgia Tech Research Institute (GTRI) turntable ISAR dataset that were acquired from a tower platform for a T-72 tank target. The collection can be publicly accessed online via the Air Force Research Laboratory (AFRL) website [35].

As described on this website, the GTRI dataset consists of a total of 29 folders each of which corresponds to full-aperture (azimuth) and full-polarimetric target signatures for a specific depression angle. Each folder holds 85 data files for each polarization and hence full-aperture is divided into 85 subapertures. For each subaperture, azimuth-stepped data were collected with 0.05° steps for a bandwidth of 3.9°, while frequency-stepped data were collected with 3 MHz steps within a range of 9.27 GHz to 9.93 GHz. Here, we have selected "f115YY8" file for which the depression angle is 30° and the target's azimuthal orientation is 35.975°. The letters YY in the filename denote one out of the 4 pairs of transmitter/receiver polarization. Note that for these X-band measurements and a full-scale $d \cong 10$ m wide target, the antenna to target distance r has to be more than 6.7 km for it to satisfy the far-field criteria $r \geq 2d^2/\lambda$ where λ being the operational wavelength. This criterion was obviously not

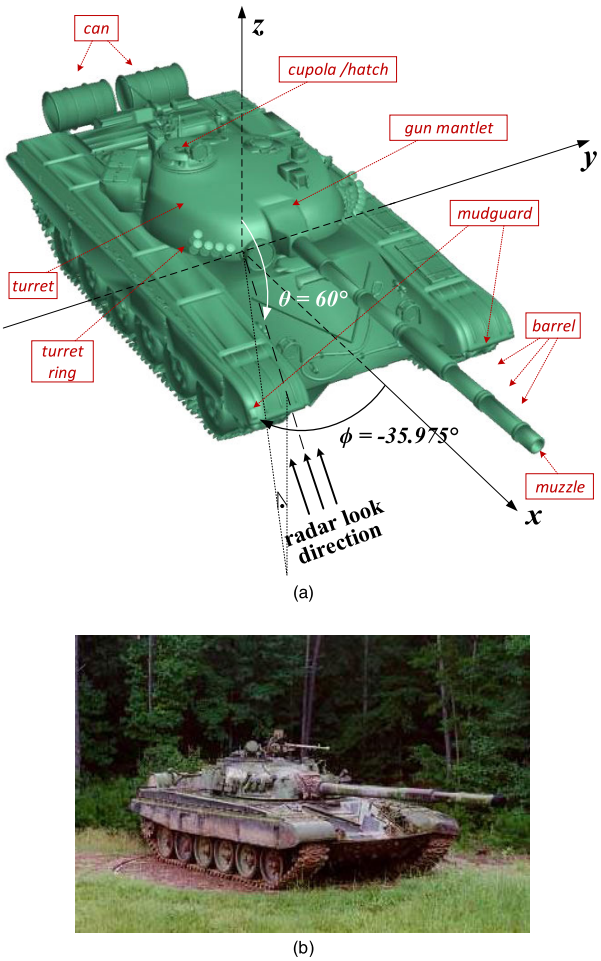

FIGURE 15. Geometry for the full-polarimetric RCS/ISAR imaging of the "T-72 tank" object for the aspect angle $\left(\theta^i = 30°, \phi^i = 35.975°\right)$. (a) Simulation, (b) real experiment.

satisfied for this tower-turntable set-up meaning that data represent near-field measurements. Therefore, RCS analyses will not be made in this section.

A far-field PREDICS simulation was also conducted with the parameters of the real experiment so that comparisons can be made. Fig. 15(a) shows the CAD model used in the simulation and the geometry of both experiments. A photograph of the target scene is shown in Fig. 15(b). For this model of T-72 tank, the turret is given in oval, hemispheric shape and connected to the hull via a turret ring. The commander cupola/hatch is situated to the right rear of the turret and composed of a machine gun and various vision blocks. Moreover, two cans are fitted to the rear plates.

In the following analyses, both the simulation and real measurement results will be given. Synthetically generated CP images and total power images will not be provided for brevity. Prior to imaging, windowing with a Hanning function and a subsequent zero padding with a factor of 4 were applied to both frequency and angular data for smoothing and interpolation purposes. For the real measurements, a zero-Doppler clutter removal procedure was also performed by finding the mean values of azimuthal data for each

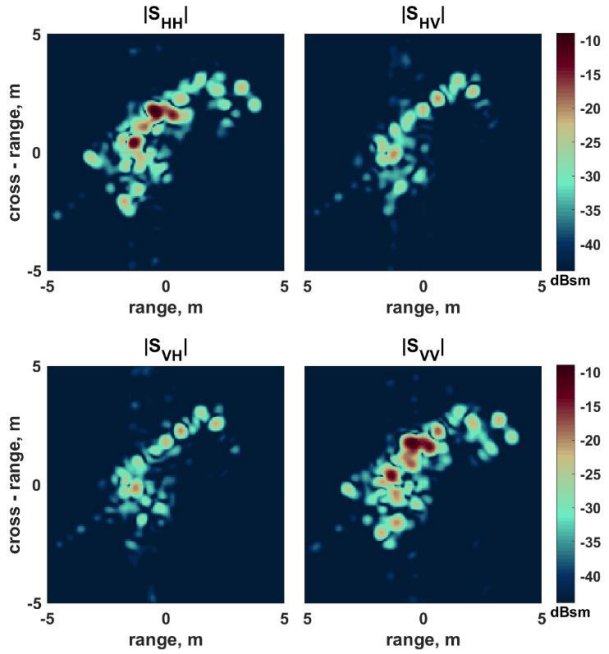

FIGURE 16. Simulated LP ISAR images of the "T-72 tank" object for the aspect angle $\left(\theta^i = 30°, \phi^i = -35.975°\right)$.

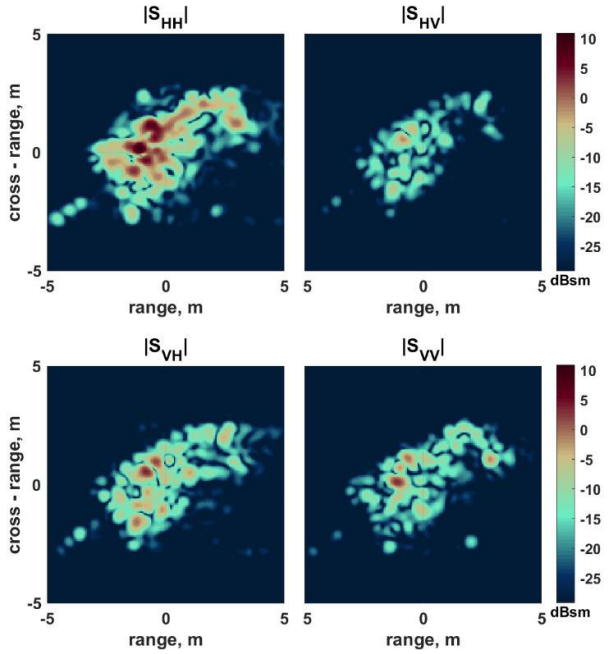

FIGURE 17. Real LP ISAR images of the "T-72 tank" object for the aspect angle $\left(\theta^i = 30°, \phi^i = -35.975°\right)$.

frequency bin and then subtracting these values from the corresponding frequency data measured at a specific azimuth angle [36]–[39].

Fig. 16 and Fig. 17 shows the reconstructed ISAR images of simulation and real data, respectively. It is worth remarking that radar backscatter from manmade targets are usually ascribed to single-, double- and multi-bounce mechanisms but not to random (diffuse) scattering mechanisms such as caused by natural media. Consequently, lower cross-pol signatures are normally expected. The oriented and asymmetric structures, however, can lead to strong cross-pol terms.

A. INTERPRETATION OF INTENSITY IMAGES

First, consider the simulation results given in Fig. 16. At a first glance, both co-pol and cross-pol images seem to exhibit similar features among themselves. Besides, co-pol powers are higher than cross-pol ones, as expected. The gun barrel/muzzle and the side of the hull facing to the radar can be readily noticed in all channels. Note that there is no backscatter from the left rear at this orientation angle. Cross-pol returns from roadwheels/tracks are due to their highly complex and partly hollow structure which would be able to produce very sophisticated scattering mechanisms. The other cross-pol returns coming from the right rear and gun barrel can be attributed to orientation since these sections are relatively simple in shape. As for the analysis of co-pol returns, the aforementioned target parts are recognized to generate co-pol returns, as well. There exists, however, additional returns from the turret, front mudguards and cans. The latter two ones are seen by radar as corner-reflectors and thus producing strong co-pol returns. For the turret section, the two adjacent hot spots are confirmed to belong to commander cupola while the other spot most probably belongs to turret ring. These major scatterings can be explained by possible corner-like and elevated structures on the turret.

Second, consider the real results given in Fig. 17. The general scattering behavior is seen as similar to that of simulation. It should be noted that while PREDICS is calculating the far-field EM scattering of the target, the measured data was for a near-field measurement. Yet, the correlation between the simulated images in Fig.16 to the measured ones in Fig. 17 is quite high.

In particular, the gun barrel/muzzle, rear and right sides and the turret section are clearly visualized in the measured polarization ISAR images. Scatterings from the turntable edges can also be noticed from $|S_{HH}|$ image. The two cans, however, are not displayed more clearly for this situation. Furthermore, real images are seen to have higher power levels than simulation ones owing to near-field operation. This might also cause real imagery to have lower $|S_{VV}|$ returns than $|S_{HH}|$ ones, as observed in Fig. 17. Nevertheless, the correlation between $|S_{HH}|$ and $|S_{VV}|$ scattering pattern is still seen to be high. To sum up, the degree of similarity between simulation and real images reflects good performance of the PREDICS simulator.

B. INTERPRETATION OF PAULI IMAGES

Pauli images of simulation and real data are shown in Fig. 18(a) and Fig. 18(b), respectively. Both images carry similar information for several target sections, as explained in the following. The gun barrel/muzzle and gun mantlet (front facing shield covering the gun) are shown up in green indicating dominance of multi-bounce scatterings. The right rear has light green and red tones implying a combination of

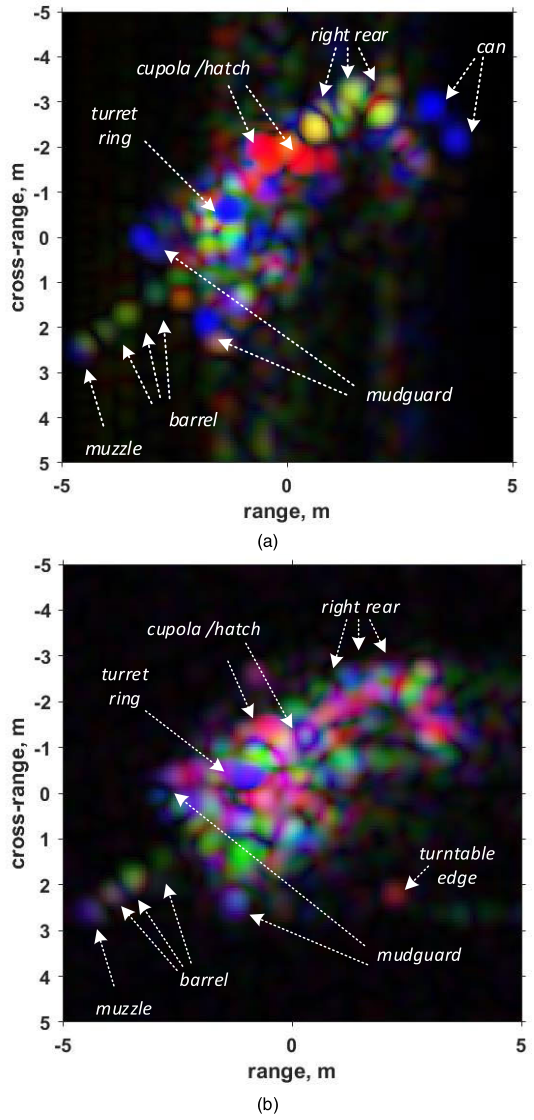

FIGURE 18. Pauli RGB image with $R = |S_{HH} - S_{VV}|$, $G = |S_{HV} + S_{VH}|$, $B = |S_{HH} + S_{VV}|$, of the "T-72 tank" object for the aspect angle $\left(\theta^i = 30°, \phi^i = -35.975°\right)$. (a) Simulation, (b) real experiment.

double- and multi-bounce mechanisms. The two front mudguards are seen as blue and purple in simulated and real images respectively. It can be commented that these sections ideally show TCR scattering but in reality they also exhibit even-bounce returns in addition to this stronger odd-bounce return. In simulated image, the two adjacent hot spots belonging to turret's commander cupola are in red indicating strong double-bounce returns due to step-like structures. In real image, these spots are displayed as magenta (red+blue) and yellow (red+green), thus are in partial agreement with simulation. The other spot belonging to turret ring is in blueish tones for each case. The two cans that are clearly visible in simulation case show TCR-like scattering as expected at this look angle. The discrepancies between simulated and real images are mostly concentrated in roadwheels/tracks and turret sections as evident from the large variation in color tones. This is reasonable since the CAD models are usually not fully representative of the actual target. Overall, both the simulated and the real ISAR Pauli images represent almost similar features as indicated in Figure 18. These comparisons of Pauli images, reveal the capability of the PREDICS simulator in predicting the actual physical scattering mechanisms.

V. CONCLUSION AND DISCUSSIONS

We have presented an assessment procedure of polarimetric ISAR imaging for classifying scattering characteristics from simple and complex targets by the help of Pauli image decomposition and interpretation scheme. The benchmark target SLICY has been used to validate the base of the classifications of coherent scattering mechanisms for single/odd, double and multiple reflections. Next, a much more realistic and complex object of a back-hoe loader have been selected to pursue extracting coherent and incoherent reflections. Fully-polarized backscattering calculations were accomplished and corresponding co-pol and cross-pol ISAR images were constructed by the help of high-frequency RCS scattering tool PREDICS. Constructing the Pauli image of back-hoe loader based on co-pol and cross-pol ISAR data have yield very interesting results that pinpoint the various scattering features such as single, double, triple and multiple bounces with and without deflected waves. Thus; using polarization decomposition techniques with appropriate interpretation in fully-polarized ISAR images provides a successful tool for classifying target features. Also, a measured data from a T72 military tank have been exploited to form the polarization images. A good agreement between the real and simulated polarization/Pauli images has been attained that further validates both the PREDICS's precise prediction of electromagnetic scattering and the analysis approach that is given in this work. Such an approach, therefore, can be effectively utilized for ISAR automatic target recognition (ATR) applications with high fidelity.

REFERENCES

[1] J. Lee and E. Pottier, *Polarimetric Radar Imaging: From Basics to Applications*. New York, NY, USA: Taylor & Francis, 2009.
[2] J. van Zyl and Y. Kim, *Synthetic Aperture Radar Polarimetry*. Hoboken, NJ, USA: Wiley, 2011.
[3] A. Moreira, P. Prats-Iraola, M. Younis, G. Krieger, I. Hajnsek, and K. P. Papathanassiou, "A tutorial on synthetic aperture radar," *IEEE Geosci. Remote Sens. Mag.*, vol. 1, no. 1, pp. 6–43, Mar. 2013.
[4] K. Ouchi, "Recent trend and advance of synthetic aperture radar with selected topics," *Remote Sens.*, vol. 5, no. 2, pp. 716–807, Feb. 2013.
[5] C. Ozdemir, *Inverse Synthetic Aperture Radar Imaging with MATLAB Algorithms* (Wiley Series in Microwave and Optical Engineering). Hoboken, NJ, USA: Wiley, 2012.
[6] E. Knott, *Radar Cross Section Measurements*. Raleigh, NC, USA: SciTech, 2006.
[7] D. L. Mensa, *High Resolution Radar Cross-Section Imaging*. Norwood, MA, USA: Artech House, 1991.
[8] N. C. Currie, Ed., *Radar Reflectivity Measurement: Techniques and Applications*. Norwood, MA, USA: Artech House, 1989.
[9] M. N. Cohen, "Variability of ultrahigh-range-resolution radar profiles and some implications for target recognition," *Proc. SPIE*, vol. 1699, pp. 256–266, Jul. 1992.
[10] C. Baird, W. Kersey, R. Giles, and W. Nixon, "Exploitation of ISAR imagery in Euler parameter space," *Proc. SPIE, Radar Sensor Technol. IX Int. Soc. Opt. Photon.*, vol. 5788, pp. 116–127, May 2005.
[11] C. Baird, W. Kersey, R. Giles, and W. Nixon, "Classification of targets using optimized ISAR Euler imagery," in *Proc. SPIE, Radar Sensor Technol. X Int. Soc. Opt. Photon.*, vol. 6210, pp. 1–12, May 2006.

[12] C. S. Baird, "Design and analysis of an Euler transformation algorithm applied to full-polarimetric ISAR imagery," Ph.D. dissertation, Dept. Phys., Univ. Massachusetts Lowell, Lowell, MA, USA, 2007.
[13] C. Baird, W. T. Kersey, R. Giles, and W. E. Nixon, "Classification of targets using optimized ISAR Euler imagery," Submillim.-Wave Technol. Lab., Univ. Massachusetts Lowell, Lowell, MA, Tech. Rep. AD-A462979, May 2006.
[14] T. Dallmann and D. Heberling, "Discrimination of scattering mechanisms via polarimetric RCS imaging [measurements corner]," *IEEE Antennas Propag. Mag.*, vol. 56, no. 3, pp. 154–165, Jun. 2014.
[15] T. Dallmann and D. Heberling, "Principal component analysis for polarimetric radar cross-section imaging," in *Proc. 10th Eur. Conf. Antennas Propag. (EuCAP)*, Apr. 2016, pp. 1–5.
[16] T. Dallmann and D. Heberling, "Technique for Huynen–Euler decomposition," *Electron. Lett.*, vol. 53, no. 13, pp. 877–879, Jun. 2017.
[17] M. Martorella, E. Giusti, L. Demi, Z. Zhou, A. Cacciamano, F. Berizzi, and B. Bates, "Target recognition by means of polarimetric ISAR images," *IEEE Trans. Aerosp. Electron. Syst.*, vol. 47, no. 1, pp. 225–239, Jan. 2011.
[18] M. Martorella, A. Cacciamano, E. Giusti, F. Berizzi, B. Haywood, and B. Bates, "CLEAN technique for polarimetric ISAR," *Int. J. Navigat. Observ.*, vol. 2008, Jan. 2008, Art. no. 325279.
[19] M. Duquenoy, J. P. Ovarlez, L. Ferro-Famil, L. Vignaud, and E. Pottier, "Study of dispersive and anisotropic scatterers behavior in radar imaging using time-frequency analysis and polarimetric coherent decomposition," in *Proc. IEEE Conf. Radar*, Jun. 2006, pp. 180–185.
[20] M. Duquenoy, J. P. Ovarlez, L. Ferro-Famil, E. Pottier, and L. Vignaud, "Scatterers characterisation in radar imaging using joint time-frequency analysis and polarimetric coherent decompositions," *IET Radar, Sonar Navigat.*, vol. 4, no. 3, pp. 384–402, Jun. 2010.
[21] T. Dallmann, "Polarimetric radar cross-section imaging," Ph.D. dissertation, Dept. Elect. Eng. Inf. Technol., RWTH Aachen Univ., Aachen, Germany, 2017.
[22] S. R. Cloude and E. Pottier, "A review of target decomposition theorems in radar polarimetry," *IEEE Trans. Geosci. Remote Sens.*, vol. 34, no. 2, pp. 498–518, Mar. 1996.
[23] J.-S. Lee and T. L. Ainsworth, "An overview of recent advances in polarimetric SAR information extraction: Algorithms and applications," in *Proc. IEEE Int. Geosci. Remote Sens. Symp.*, Honolulu, HI, USA, Jul. 2010, pp. 25–30.
[24] S.-W. Chen, Y.-Z. Li, X.-S. Wang, S.-P. Xiao, and M. Sato, "Modeling and interpretation of scattering mechanisms in polarimetric synthetic aperture radar: Advances and perspectives," *IEEE Signal Process. Mag.*, vol. 31, no. 4, pp. 79–89, Jul. 2014.
[25] S. W. Chen, X. S. Wang, S. P. Xiao, and M. Sato, "Advanced polarimetric target decomposition," in *Target Scattering Mechanism in Polarimetric Synthetic Aperture Radar*. Singapore: Springer, 2018, ch. 2, pp. 43–106.
[26] V. Alberga, E. Krogager, M. Chandra, and G. Wanielik, "Potential of coherent decompositions in SAR polarimetry and interferometry," in *Proc. IEEE Int. Geosci. Remote Sens. Symp.*, Anchorage, AK, USA, Sep. 2004, pp. 1792–1795.
[27] O. Kirik and C. Ozdemir, "An accurate and effective implementation of physical theory of diffraction to the shooting and bouncing ray method via predics tool," *Sigma J. Eng. Natural Sci.*, vol. 37, no. 4, pp. 1149–1162, 2019.
[28] C. Özdemir, B. Yilmaz, and Ö. Kirik, "PRediCS: A new GO-PO-based ray launching simulator for the calculation of electromagnetic scattering and RCS from electrically large and complex structures," *TURKISH J. Electr. Eng. Comput. Sci.*, vol. 22, pp. 1255–1269, 2014.
[29] C. Ozdemir, O. Kirik, B. Yilmaz, and O. Sutcuoglu, "A fast and efficient RCS calculation and ISAR image formation tool: pRediCS," in *Proc. 10th Eur. Conf. Synth. Aperture Radar (EUSAR)*, Berlin, Germany, Jun. 2014, pp. 1–4.
[30] F. Weinmann and J. Nitschkowski, "A SBR simulator with GO-PO for calculating scattered fields from coated surfaces," in *Proc. 4th Eur. Conf. Antennas Propag.*, Barcelona, Spain, Apr. 2010, pp. 1–4.
[31] H. Wu, B. Pang, D. Dai, J. Wu, and X. Wang, "Unmanned aerial vehicle recognition based on clustering by fast search and find of density peaks (CFSFDP) with polarimetric decomposition," *Electronics*, vol. 7, no. 12, p. 364, Dec. 2018.
[32] Q. Liu, C. Pang, Y. Li, and X. Wang, "Impact of polarization distortions on geometrical structure retrieval of moving man-made targets in ISAR images," *Electronics*, vol. 8, no. 4, p. 373, Mar. 2019.
[33] H. Ling, R.-C. Chou, and S.-W. Lee, "Shooting and bouncing rays: Calculating the RCS of an arbitrarily shaped cavity," *IEEE Trans. Antennas Propag.*, vol. 37, no. 2, pp. 194–205, Feb. 1989.
[34] H. Ling, S.-W. Lee, and R.-C. Chou, "High-frequency RCS of open cavities with rectangular and circular cross sections," *IEEE Trans. Antennas Propag.*, vol. 37, no. 5, pp. 648–654, May 1989.
[35] U.S. Air Force, Sensor Data Management System (SDMS). (1997). *GTRI Dataset*. [Online]. Available: https://www.sdms.afrl.af.mil/index.php?collection=gtri
[36] G. A. Showman, K. J. Sangston, and M. A. Richards, "Correction of artifacts in turntable inverse synthetic aperture radar images," *Proc. SPIE, Int. Soc. Opt. Eng.*, vol. 3066, pp. 40–51, Apr. 1997.
[37] G. A. Showman, M. A. Richards, and K. J. Sangston, "Comparison of two algorithms for correcting zero-Doppler clutter in turntable ISAR imagery," in *Proc. Conf. Rec. 32nd Asilomar Conf. Signals, Syst. Comput.*, Pacific Grove, CA, USA, vol. 1, 1998, pp. 411–415.
[38] J. D. Fowler, M. A. Temple, M. J. Havrilla, and J. J. Akerson, "Characterization of zero-Doppler clutter removal techniques for ISAR applications," in *Proc. IEEE Radar Conf.*, Boston, MA, USA, Apr. 2007, pp. 800–804.
[39] L. Yu and Y. Zhang, "CSAR imaging with data extrapolation and approximate GLRT techniques," *Prog. Electromagn. Res. M*, vol. 19, pp. 209–220, 2011, doi: 10.2528/PIERM11062904.

SEVKET DEMIRCI received the B.S. degree from Çukurova University, Adana, Turkey, in 1998, and the M.S. and Ph.D. degrees from Mersin University, Mersin, Turkey, in 2005 and 2013, respectively, all in electrical and electronics engineering. He is currently an Assistant Professor with the Department of Electrical and Electronics Engineering, Mersin University. His current research interests include radar engineering, synthetic aperture radar (SAR), ground penetrating radar (GPR), polarimetric SAR, target detection techniques, and compressive sensing.

OZKAN KIRIK received the B.S. and M.S. degrees from Mersin University, Mersin, Turkey, in 2006 and 2009, respectively, all in electrical and electronics engineering, where he is currently pursuing the Ph.D. degree in electrical and electronics engineering. He is also a Lecturer with Mersin University. His current research interests include radar engineering, inverse synthetic aperture radar (ISAR), radar image/signal processing, radar cross section, and parallel computing.

CANER OZDEMIR (Member, IEEE) received the B.S.E.E. degree from Middle East Technical University, Ankara, Turkey, in 1992, and the M.S.E. and Ph.D. degrees in electrical and computer engineering from The University of Texas at Austin, in 1995 and 1998, respectively. From 1992 to 1993, he worked as a Project Engineer at the Electronic Warfare Programs Directorate, ASELSAN Electronic Industries Inc., Ankara. From 1998 to 2000, he worked as a Research Scientist at the Electronic and Avionics Systems (ASTG) Group, AlliedSignal Inc., Columbia, Maryland. He joined Mersin University, Mersin, Turkey, as a Faculty Member, in 2000, where he is currently a Professor with the Department of Electrical and Electronics Engineering. He has been serving as a Consultant for the Marmara Research Center of the Scientific and Research Council (TUBITAK), Turkey, and many defense industry firms. He is the author of the book titled *Inverse Synthetic Aperture Radar Imaging With MATLAB Algorithms*. His research interests include radar image/signal processing, inverse synthetic aperture radar (ISAR), radar cross section, ground penetrating radar, through-the-wall imaging radar, and antenna design. He has published more than 150 journal articles and conference/symposium papers on these subjects. He was a recipient of the URSI EMT-S Young Scientist Award at the 2004 International Symposium on Electromagnetic Theory, Pisa, Italy, and the JARS Best Paper Award for photo-optical instrumentation published in the *Journal of Applied Remote Sensing*, in 2016.